Research Article | Vol. 33, No. 12 / 16 Jun 2025 / Optics Express 25221
Optics EXPRESS

Fast and compact four-quadrant CEP detection with *f*-2*f* polarization interferometry

SIMON MAIER,[1] MANUEL MEIERHOFER,[1] IGNAZ LAEPPLE,[1] KATHARINA GLÖCKL,[1] CHRISTOPH TRESP,[2] MATTHIAS HOHENLEUTNER,[2] MARKUS A. HUBER,[1] AND RUPERT HUBER[1,*]

[1]*Department of Physics, and Regensburg Center for Ultrafast Nanoscopy (RUN), University of Regensburg, 93040 Regensburg, Germany*
[2]*TOPTICA Photonics AG, 82166 Gräfelfing, Germany*
[*]*rupert.huber@physik.uni-regensburg.de*

Abstract: The carrier-envelope phase (φ_{CEP}) of few-cycle light pulses is of crucial importance for strong-field light-matter interaction on subcycle time scales. Standard *f*-2*f* interferometry rapidly records beat notes defined by the carrier-envelope offset frequency (f_{CEO}), but measuring φ_{CEP} at a high bandwidth is more involved. Here, we introduce *f*-2*f* polarization interferometry, which unambiguously measures φ_{CEP} over a range of 2π at the detection speed of the implemented photodiodes. It relies on evaluating the polarization state of the spectral overlap of a traditional *f*-2*f* interferometer with linear optical components and balanced photodiodes. In the first implementation, we detect φ_{CEP} modulations with a read-out rate of up to 60 kHz. Our scheme promises single-shot φ_{CEP} detection at intrinsic oscillator repetition rates in the MHz regime. It can be used in a wide range of ultrafast experiments, from φ_{CEP} stabilization and phase tagging to selective high-harmonic generation and precise lightwave control of electron motion.

The development of ultrabroadband laser sources has revolutionized precision metrology in both the time and the frequency domain. Pulse lengths down to less than a single oscillation cycle of light call for a reliable and fast determination of the phase between carrier wave and pulse envelope called the carrier-envelope phase (φ_{CEP}). The strong influence of φ_{CEP} on non-perturbative nonlinearities has been demonstrated experimentally over a broad frequency spectrum, from visible to far infrared pulses [1–13]. The CEP of few-cycle pulses determines high-harmonic generation (HHG) in gases [1–5] and, consequently, the emission of single attosecond light pulses, which led to the Nobel Prize in Physics 2023. In solids, this idea has sparked the field of lightwave electronics [6]. The recent exploration of high-harmonic generation in solids requires a precise knowledge of the CEP of the mid-infrared driving pulse [7]. In addition, field emission and lightwave-driven tunneling in nanostructures are governed by φ_{CEP}, enabling the generation of femtosecond (fs) and sub-fs electron wave packets, eventually leading to the development of electronics at optical clock rates [6,8–13]. Hence, controlling the CEP means shaping electron motion on its intrinsic time scale. Therefore, real-time, single-shot, and easy-to-use CEP detection is imperative for future precision metrology in the time domain as well as optoelectronic applications.

Waveform-sampling methods like electro-optic sampling [14,15] or strong-field effects [16,17] can provide absolute carrier-envelope phase information. In most cases, it is sufficient to trace relative changes of φ_{CEP} as accessible with interferometric methods [18]. The phase change $\Delta\varphi_{CEP}$ from pulse-to-pulse is proportional to the carrier-envelope offset frequency $f_{CEO} = \frac{\Delta\varphi_{CEP}}{2\pi} f_{rep}$, with the repetition rate f_{rep}. Seminal works on *f*-2*f* interferometry have demonstrated detection of the beat note corresponding to f_{CEO} with a single photodetector [18,19]. These works have triggered the development of a plethora of CEP detection schemes owing to the diversity of applications. For many applications it is required to trace the change in φ_{CEP} itself. The approach of Ref.

#545392 https://doi.org/10.1364/OE.545392
Journal © 2025 Received 16 Oct 2024; revised 9 Apr 2025; accepted 13 Apr 2025; published 5 Jun 2025

Optics EXPRESS

[19] is also applicable for phase detection of zero-offset combs by including an acousto-optic modulator (AOM) into the $2f$-arm of the interferometer. To infer the CEP from the spectrally modulated interferogram [20], typically a grating spectrometer with a photodetector array (CMOS or CCD) and a software-based fast Fourier transform (FFT) are necessary. In these cases, the read-out frequency of the photodetector chip and the software-based FFT limit the speed to the millisecond range.

Recent attempts have successfully increased the bandwidth of this approach above 100 kHz: to this end, the FFT has been performed with optimized electronics [21], or the interferogram has either been recorded with a high-speed line camera [22] or dispersed in time to become detectable with a single-pixel photodetector [23] potentially enabling CEP sampling at tens of MHz [24]. Another approach to improve the bandwidth is to measure the CEP-dependent differences in spectral weight of two parts of the interferogram with a pair of photodetectors [25]. Along this line, Liehl *et al.* employed a balanced pair of photodiodes and demonstrated CEP detection at 50 MHz, the Nyquist frequency of the used oscillator [26]. In this configuration, the sinusoidal signal enables unambiguous detection in a window of π. Recently, a detection scheme has been published that covers the full phase range of 2π at a single-shot rate with a bandwidth of 200 kHz [27]. This approach has employed a sophisticated Michelson interferometer to retrieve the phase information from the spectral f-$2f$-interferogram via an optical Fourier transform. Fast photodiode-based detection and only a few necessary arithmetic steps to calculate the phase call for a potentially higher detection bandwidth up to tens of MHz. Yet, the phase detection relies on a perfect adjustment of the path length of the Michelson interferometer, where small changes can be misinterpreted as changes in the CEP. Finally, the CEP can also be inferred with different techniques such as field emission from nanoantennas [12] or above-threshold ionization in gases [17]. To date, most spectral CEP detection methods are either broadband but have a limited detection range of π, or they discriminate phases over the entire 2π range but are limited to a detection bandwidth of a few hundred kHz by design. It would be desirable to develop a CEP detection scheme which works over 2π at the desired electronic bandwidth, is easy to set up and cost-efficient, and is robust against thermal drift and noise.

Here, we present a CEP detection technique that allows us to measure φ_{CEP} over all four quadrants (from 0 to 2π) in a straightforward and linear fashion. It is based on encoding φ_{CEP} onto the polarization state of light via f-$2f$ interference of two spectral wings of an ultrashort laser pulse and subsequent analysis of the polarization state using balanced photodiodes. The scheme can readily be applied to zero-offset combs without involving additional frequency shifters in the interferometer. The detection speed is solely determined by the bandwidth of the photodiodes. In our proof-of-principle implementation shown here, without any further optimization, we reach a bandwidth of 60 kHz, already competing with the above-described methods [21–23,25,27]. This can easily be extended using faster silicon photodetectors enabling single-shot detection at high-frequency oscillator repetition rates (tens of MHz). Hence, the method enables broadband CEP control of lasers as well as CEP tagging of free-running oscillators, which have been unable to access CEP-dependent phenomena so far. Our implementation is insensitive to drift since it is based on a common-path geometry. We present the measurement scheme followed by one real implementation which is used to perform a proof-of-principle measurement. Furthermore, we test our approach in a PID feedback loop and detect a square-like modulated CEP.

To introduce our conceptual idea, we revisit the foundations of f-$2f$ interferometry for an exemplary phase-stable ultrafast laser source, which can also be described mathematically as an offset-free frequency comb (Fig. 1(a)). The comb lines are integer multiples n of the repetition rate f_{rep}. For an over-octave-spanning spectrum, frequencies at $n \times f_{\mathrm{rep}}$ (red line) in the low-frequency part of the comb can be doubled in a nonlinear crystal and yield comb lines (blue dashed line) still within the full spectrum of the pulse. For type-I phase matching, the newly generated spectral components emerge orthogonally polarized. Once a polarizer projects both components onto a

Optics EXPRESS

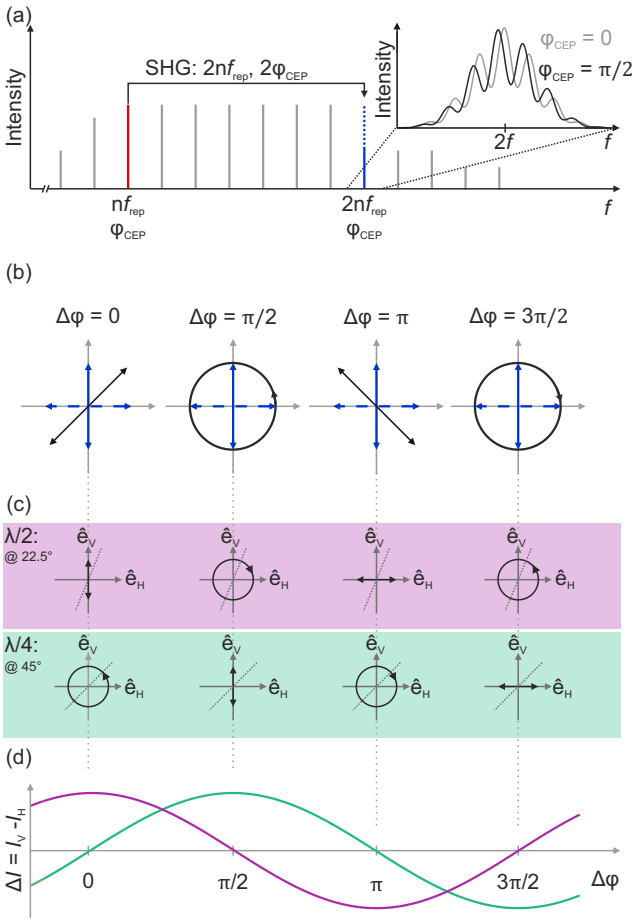

Fig. 1. Conceptual idea of f-$2f$ polarization interferometry. (a) In traditional f-$2f$ interferometry, the spectral interference between a frequency-doubled (SHG) long-wavelength part around nf_{rep} of an octave-spanning frequency comb and a short-wavelength part around $2nf_{\mathrm{rep}}$ results in spectral fringes, whose positions depend on the CEP (inset). (b) In contrast, f-$2f$ polarization interferometry exploits the CEP-dependent polarization state of the two superimposed and cross-polarized fields. Depending on the CEP, the polarization can continuously vary between linear, elliptical, and circular. (c) Polarization state of the superimposed fields after transmission through a half-wave plate (λ/2) at an angle of 22.5° (purple) or a quarter-wave plate (λ/4) at an angle of 45° (green) with respect to the vertical axis. (d) Sine- and cosine-shaped signals generated by analyzing the polarization states of (c) with a Wollaston prism and balanced photodiodes.

common axis, the newly generated wave at $2nf_{\mathrm{rep}}$ can interfere with an existing comb line and forms the typical f-$2f$ interferogram (Fig. 1(a), inset). The phase of the second harmonic scales with $2\times\varphi_{\mathrm{CEP}}$, which is twice the value of the fundamental wave, leading to a phase difference of $\Delta\varphi=\varphi_{\mathrm{CEP}}+\psi$, where ψ is a constant offset caused by dispersion and birefringence. The interferogram behaves like $I(f,\Delta\varphi)\propto\cos(2\pi f\tau+\Delta\varphi)$, where τ is the time delay between the two interfering pulses. Consequently, the spectral maxima and minima of the interferogram shift with φ_{CEP} as illustrated for exemplary values of 0 and π/2.

Instead of imprinting the CEP in a spectral signature, it can also be encoded in the polarization state after the f-$2f$ interferometer [28]. Figure 1(b) illustrates the polarization state after the

Optics EXPRESS

crystal for selected phase differences $\Delta\varphi = \varphi_{\mathrm{CEP}} + \psi$ when no polarizer is inserted. For simplicity, we start by assuming equal field strengths of the interfering f and $2f$ components and treat the general case later.

The offset ψ is constant in time and therefore omitted in the following discussion. The fundamental wave (solid blue arrow) is vertically polarized

$$\vec{E}_f = E_0 \cos(2\pi f t + \varphi_{\mathrm{CEP}})\, \hat{\mathbf{e}}_{\mathrm{V}} \tag{1}$$

and the dashed blue arrows show the horizontally polarized second harmonic field (SHG)

$$\vec{E}_{2f} = E_{\mathrm{SHG}} \cos(2\pi 2(f/2)t + 2\varphi_{\mathrm{CEP}})\, \hat{\mathbf{e}}_{\mathrm{H}} \tag{2}$$

with horizontal and vertical unit vectors $\hat{\mathbf{e}}_{\mathrm{H}}$ and $\hat{\mathbf{e}}_{\mathrm{V}}$. Due to their crossed polarization, there is no spectral interference [28], but the polarization state changes depending on $\Delta\varphi \sim \varphi_{\mathrm{CEP}}$. When $\Delta\varphi = 0$ or π the superimposed field is linearly polarized

$$\vec{E}_{\mathrm{total}} = (E_{\mathrm{SHG}}\, \hat{\mathbf{e}}_{\mathrm{H}} \pm E_0\, \hat{\mathbf{e}}_{\mathrm{V}}) \cos(2\pi f t). \tag{3}$$

For $\varphi_{\mathrm{CEP}} = \pi/2$ or $3\pi/2$, right- or left-hand circularly polarized light is formed

$$\vec{E}_{\mathrm{total}} = -E_{\mathrm{SHG}} \cos(2\pi f t)\, \hat{\mathbf{e}}_{\mathrm{H}} \pm E_0 \sin(2\pi f t)\, \hat{\mathbf{e}}_{\mathrm{V}}. \tag{4}$$

For every other CEP value, elliptically polarized light emerges from the crystal. By analyzing the polarization state, the CEP can be inferred over its full range of 2π.

The fundamental principle of this retrieval is schematically explained in Figs. 1(c) and (d) and is solely based on two wave plates and simple polarization optics. When transmitting $\vec{E}_{\mathrm{total}}$ through a half-wave plate ($\lambda/2$) at an angle of $\Theta = 22.5°$ with respect to the vertical axis, the polarization is rotated accordingly. Four exemplary cases are illustrated in the purple box, with the dashed line as the axis of the half-wave plate. To extract the phase, we need to consider the difference in intensities between horizontal and vertical axes (purple line in d). To this end, the output after the $\lambda/2$ plate needs to be projected onto the horizontal and vertical axis (e.g. by a Wollaston prism), measured, and subtracted. The corresponding signal is proportional to $\Delta I_{\lambda/2} \sim \cos(\varphi_{\mathrm{CEP}})$. With this setup, a change in CEP by π can be measured unambiguously. To cover the full range of 2π, we also need to detect the Hilbert transform of the signal, i.e., a signal that is shifted by $\pi/2$. We achieve this goal by using a quarter-wave plate ($\lambda/4$) rotated by $\Theta = 45°$ with respect to the vertical axis (Fig. 1(c), green box; Fig. 1(d), green line). In this case, the difference of polarizations follows $\Delta I_{\lambda/4} \sim \sin(\varphi_{\mathrm{CEP}})$. The same arguments hold if $\varphi_{\mathrm{CEP}}(t)$ varies from shot-to-shot as a function of time.

For the case of arbitrary amplitudes of E_0 and E_{SHG}, the same relations hold, which can be shown using the Jones formalism for polarization matrices, starting with the initial polarization state $\vec{J}_{\mathrm{in}} = \begin{pmatrix} E_{\mathrm{SHG}} e^{-i2\varphi_{\mathrm{CEP}}} & E_0 e^{-i\varphi_{\mathrm{CEP}}} \end{pmatrix}$. The matrices for retardation plates at the respective angles read [29]

$$M_{\lambda/2}(\Theta = \pi/8) = 1/\sqrt{2} \begin{pmatrix} 1 & 1 \\ 1 & -1 \end{pmatrix} \tag{5}$$

and

$$M_{\lambda/4}(\Theta = \pi/4) = 1/2 \begin{pmatrix} 1 - i & 1 + i \\ 1 + i & 1 - i \end{pmatrix}. \tag{6}$$

The matrices for transmitting linear polarizers are given by

$$T_{\updownarrow} = \begin{pmatrix} 0 & 0 \\ 0 & 1 \end{pmatrix} \qquad \text{and} \qquad T_{\leftrightarrow} = \begin{pmatrix} 1 & 0 \\ 0 & 0 \end{pmatrix}. \tag{7}$$

Optics EXPRESS

For the experimental conditions described above, the horizontal and vertical field components after the retardation plate (j = λ/2 or λ/4) and the polarizer can be described as

$$J_{\updownarrow,\,\mathrm{j}} = T_{\updownarrow} \cdot M_{\mathrm{j}} \cdot \vec{J}_{\mathrm{in}} \qquad \text{and} \qquad J_{\leftrightarrow,\,\mathrm{j}} = T_{\leftrightarrow} \cdot M_{\mathrm{j}} \cdot \vec{J}_{\mathrm{in}}. \tag{8}$$

We now calculate the differences in intensities of the horizontal and vertical components for each waveplate:

$$\Delta I_{\lambda/2} \propto |J_{\leftrightarrow,\lambda/2}|^2 - |J_{\updownarrow,\lambda/2}|^2 \tag{9}$$

$$\Delta I_{\lambda/4} \propto |J_{\leftrightarrow,\lambda/4}|^2 - |J_{\updownarrow,\lambda/4}|^2. \tag{10}$$

By employing the Jones calculus, one finds for arbitrary field amplitudes:

$$\Delta I_{\lambda/2} = A_{\lambda/2} \cos(\varphi_{\mathrm{CEP}}) \propto 2E_{\mathrm{SHG}}E_0 \cos(\varphi_{\mathrm{CEP}}) \tag{11}$$

and

$$\Delta I_{\lambda/4} = A_{\lambda/4} \sin(\varphi_{\mathrm{CEP}}) \propto 2E_{\mathrm{SHG}}E_0 \sin(\varphi_{\mathrm{CEP}}) \tag{12}$$

with normalization amplitudes $A_{\lambda/2}$ and $A_{\lambda/4}$. Equations (11) and (12) confirm the finding of Fig. 1(d) for arbitrary field amplitudes. The above relations hold for the perfect angles of $\Theta = \pi/8$ and $\pi/4$, for the half- and quarter-waveplates, respectively. However, the detection scheme is also robust against deviations from these angles. By performing the above calculations [Eq. (5)–(12)] for arbitrary rotation angles Θ of the retardation plates one sees that deviations only lead to a rescaling, phase shift, or offset of $\Delta I_{\lambda/2}$ and $\Delta I_{\lambda/4}$ (see Supplement 1). In practice, all of these imperfections can be eliminated by a calibration measurement and simple arithmetic steps, as we will see in our proof-of-principle measurements. Therefore, the measured $\Delta I_{\lambda/2}$ and $\Delta I_{\lambda/4}$ do not need to be exactly offset by $\pi/2$ for the phase retrieval to work from 0 to 2π.

We first implement and test this detection scheme with the setup shown in Fig. 2(a). Our laser is based on a femtosecond Er:fiber oscillator–amplifier system (TOPTICA DFC CORE). Due to intrapulse difference frequency mixing, it generates an inherently CEP-stable pulse train [30] at a repetition rate of 80 MHz with a central wavelength of 1560 nm [31]. An acousto-optic phase shifter is used to precisely control the value of the CEP [32,33]. Subsequently, the power is amplified in a dual-stage Er:fiber amplifier to 500 mW. A fraction is spectrally broadened in a highly nonlinear fiber into an over-octave-spanning spectrum (Fig. 2(b)) [34], which is well suited for f-2f interferometry with large spectral amplitudes around 150 THz (red) and 300 THz (blue). The total output power (pulse energy) is 118 mW (1.5 nJ) of which 26.6 mW (325 pJ) lie in the spectral window above 200 THz and 40.4 mW (505 pJ) in the range below 180 THz. The octave-spanning spectrum is s-polarized after the laser (Fig. 2(a)). In our common-path f-2f interferometer, we use a CaF_2 lens with a focal length of 5 cm to focus the light into a 2 mm type-I BBO crystal. The crystal is cut ($\theta = 20.3°$, $\varphi = 90°$) and rotated such that only light around a wavelength of 2 µm (150 THz) is frequency doubled. The rest of the spectrum is not phase-matched and therefore simply transmitted through the crystal. After the crystal, the fundamental (solid blue line) and second harmonic (dashed blue line) are recollimated with a fused silica lens of a focal length of 5 cm. A bandpass filter (BP) (1064 nm $\triangleq$ 282 THz, $\Delta\lambda = 25$ nm) selects the relevant frequency range to minimize unwanted background radiation. After the bandpass filter, the pulse energy amounts to 275 pJ containing both the original 2f-component and the second harmonic.

In our case, the f- and 2f-components overlap in time, rendering any additional delay control unneccessary. It is beneficial that BBO and CaF_2 exhibit close to zero dispersion around 1500 nm. For other center wavelength or laser systems delay control can be implemented within the common path geometry, either by adding a block of material of known dispersion before the lens f_1 or by adding birefringent material (e.g. calcite) after the SHG and before the beamsplitter to tune the delay between s- and p-polarized light.

Optics EXPRESS

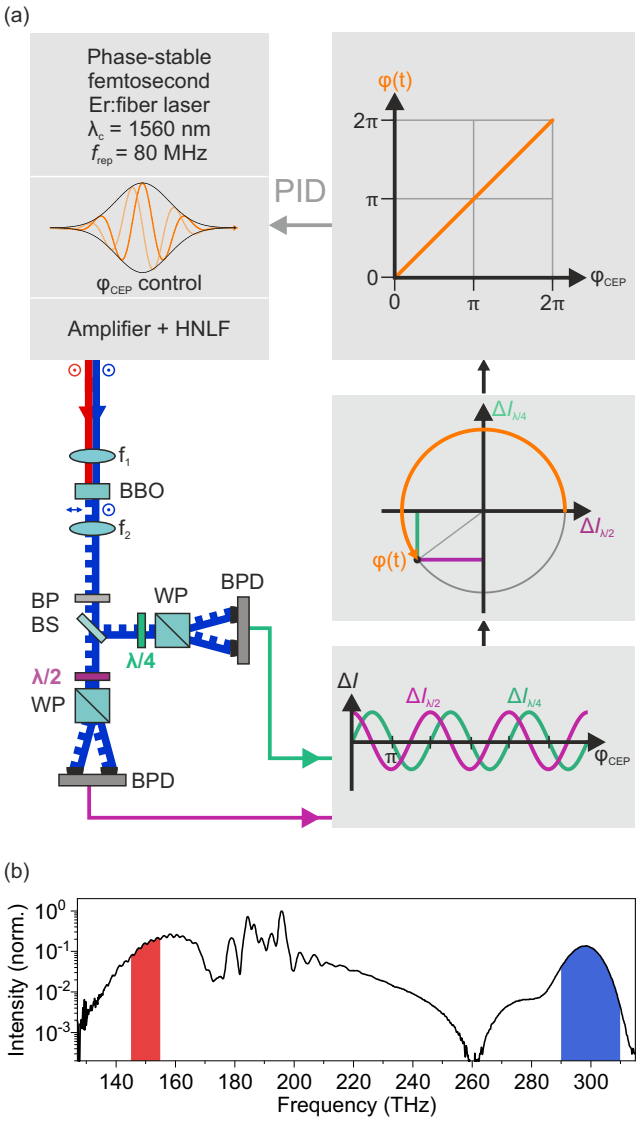

Fig. 2. Experimental scheme. (a) The output of a CEP-controlled femtosecond Er:fiber laser system is first amplified and then spectrally broadened in a highly nonlinear fiber (HNLF). A lens (f_1) focuses the light into a BBO, where the long-wavelength part (red) is frequency-doubled in a type-I geometry. A second lens (f_2) collimates the now orthogonally polarized fundamental (blue) and SHG (dashed blue) beams. Subsequently, a bandpass filter (BP) selects the spectral overlap of both pulse trains. The remaining light is split 50:50 by a nonpolarizing beamsplitter (BS). The polarization state is characterized by a combination of a quarter-wave (λ/4) and half-wave (λ/2) plate together with a Wollaston prism (WP) and two balanced photodiodes (BPD). The differential photocurrent (ΔI) exhibits a sine ($\Delta I_{\lambda/4}$, green) and cosine ($\Delta I_{\lambda/2}$, purple) dependence on the CEP (φ_{CEP}), respectively. When plotting both on two orthogonal axes, the polarization signal traces out a circle, where the CEP can be read off by the angle $\varphi(t)$. By using the atan2 function, a linear mapping between the φ_{CEP} and $\varphi(t)$ can be found. This signal can be fed into a PID controller, which allows it to stabilize and fully control φ_{CEP} of the ultrashort pulse train. (b) Experimentally measured spectrum at the output of the HNLF. The long- and short-wavelength parts used for f-2f polarization interferometry are highlighted in red and blue, respectively.

Optics EXPRESS

After the nonlinear crystal, the original pulse train centered at 300 THz is vertically polarized while the second harmonic (generated from the original 150 THz beam) at 300 THz is horizontally polarized. The CEP is imprinted in the polarization state of this pulse train and can therefore be measured in the above-described way. First, a non-polarizing 50:50 beam-splitter (BS) divides the beam. In each arm, the light passes through a wave plate and a Wollaston prism (WP) and is detected by a pair of balanced silicon photodiodes (BPD). In the first arm, a half-wave plate is used at an angle of $\Theta = 22.5°$ ($\pi/8$), whereas the second arm contains a quarter-wave plate at $\Theta = 45°$ ($\pi/4$). The BPDs feature an electronic bandwidth of 60 kHz.

Having both sine- ($\Delta I_{\lambda/4}$) and cosine-like ($\Delta I_{\lambda/2}$) signals determines φ_{CEP} up to a constant offset. The phase can be directly read off by plotting the signals on the X and Y coordinates of a 2D coordinate system (i.e., the complex plane), where it reaches all four quadrants (Fig. 2(a), right). By identifying

$$X = \frac{\Delta I_{\lambda/2}}{A_{\lambda/2}} \tag{13}$$

and

$$Y = \frac{\Delta I_{\lambda/4}}{A_{\lambda/4}} \tag{14}$$

we find

$$e^{i\varphi_{\mathrm{CEP}}} = \cos(\varphi_{\mathrm{CEP}}) + i\sin(\varphi_{\mathrm{CEP}}) = X + iY. \tag{15}$$

Hence, the arithmetic function $\varphi = \mathrm{arctan2}(X, Y)$ effectively yields φ_{CEP}. According to Eq. (11) and (12), $\Delta I_{\lambda/4}$ and $\Delta I_{\lambda/2}$ scale equally with the field amplitudes E_{SHG} and E_0. Consequently, a change in one of them only changes the radius of the circle in the complex plane, but the phase stays the same, i.e., intensity and phase fluctuations are perpendicular to each other. This makes our CEP retrieval insensitive to power fluctuations. Moreover, our implementation utilizes an all-common-path geometry in the sense that the interfering fundamental and second harmonic waves always follow the same beam path. This renders our concept very robust against drift and air turbulences.

To test our detection scheme, the phase shifter in the laser is programmed to sweep φ_{CEP} linearly in time according to $\varphi_{\mathrm{CEP}} = 2\pi f_{\mathrm{CEO}} t$, where $f_{\mathrm{CEO}} = 100$ Hz. Mathematically, all frequency comb lines get shifted by f_{CEO} (Fig. 3(a)). The blue line at $2nf_{\mathrm{rep}} + f_{\mathrm{CEO}}$ and the dashed blue (second harmonic) at $2nf_{\mathrm{rep}} + 2f_{\mathrm{CEO}}$ interfere and form a constantly shifting polarization state, which is measured with the setup of Fig. 2(a). The normalized balanced photodiode signals in Fig. 3(b) beautifully show the analytically derived signal shape. The data are sampled at a rate of 10 MS/s, which is well above the bandwidth of the BPDs. In addition, the AD-conversion is synchronized to the laser repetition rate with a 10 MHz reference signal. For clarity, we reduce the amount of shown data points by averaging 1000 (= 0.1 ms) consecutive sampling points. The data points describe sinusoidal functions of time and thus of φ_{CEP}. The normalized signals are shown in purple for the half-wave plate and gray for the quarter-wave plate.

The two signals are offset by 0.42π which deviates from the expected phase-shift of $\pi/2$. This discrepancy can be attributed to imperfections of the beamsplitter or deviations from the perfect angles Θ, which leads to an ellipse instead of a circle in the complex plane. However, $\Delta I^{\mathrm{raw}}_{\lambda/4}$ (gray) can be projected onto the Y-axis of the complex plane by using the trigonometric identity

$$\sin(x + y) = \sin x \cos y + \cos x \sin y \tag{16}$$

leading to a simple arithmetic step

$$\sin(\varphi_{\mathrm{CEP}}) = [\Delta I^{\mathrm{raw}}_{\lambda/4} - \Delta I_{\lambda/2} \ \sin\delta]/\cos\delta = \Delta I_{\lambda/4}, \tag{17}$$

where δ is a constant correction angle. The corrected signal $\Delta I_{\lambda/4}$ is shown in green in Fig. 3(b).

Optics EXPRESS

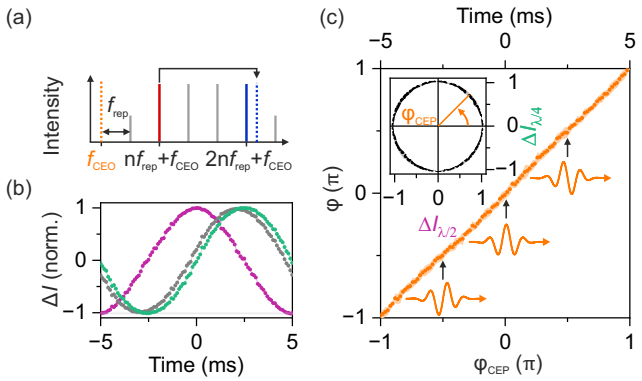

Fig. 3. Proof of principle. (a) Applying a time-dependent phase to the frequency comb of the laser pulse train shifts its line spectrum by the carrier-envelope offset frequency (f_{CEO}), which corresponds to a linearly changing φ_{CEP}. (b) Measured differential photocurrent for the half-wave (purple) and quarter-wave (gray and green) plate setups when f_{CEO} is set to 100 Hz. (c) The retrieved phase $\varphi(t)$ as a function of $\varphi_{CEP}(t)$. The measurement proves the linearity of our detection scheme over 2π. Inset: Differential photocurrents from (b) on the X-Y-plane form a circle. The angle of each data point with respect to the X-axis is proportional to φ_{CEP}.

Hence, arbitrary phase shifts in the setup can be corrected if $\delta \neq n\pi$, i.e., the zero crossings of X and Y are not identical. The exact value of δ can be determined in a calibration measurement alongside the normalization factors $A_{\lambda/2}$ and $A_{\lambda/4}$. The three parameters are optimized such that the gray ellipse approaches a circle of radius unity (Fig. 3(c), inset). From here, only the phase angle relative to the real axis must be calculated to get φ_{CEP}. Numerically retrieving $\varphi(t)$ as a function of time for every data point with a Python script yields the linear curve in Fig. 3(c). It perfectly matches the expected linear CEP slip for $f_{CEO} = 100$ Hz. The standard deviation is shown in the transparent orange background. The orange single-cycle waveforms illustrate the change in the electric field when sweeping the CEP. The resolution of the phase evaluation of our proof-of-principle implementation is approximately 0.5 mrad, which is governed by the ADC bit depth.

Having proven the linearity of our scheme, we now show its versatility with two applications. First, we reset the CEO frequency of the laser to $f_{CEO} = 0$ and trace the remaining long-term fluctuations in CEP over 4.5 hours. This is shown in orange in Figs. 4(a) and (b), reaching a passive long-term stability of $\sigma = 292$ mrad. The CEP is calculated live and batchwise with a Python script and subsequently logged. The data points are integrated for 20.7 ms each and acquired over 4.5 h (62 µHz – 24.2 Hz). While the remaining phase jitter is dominated by comparably slow fluctuations, indicating thermal influences on the fiber setup after the DFG comb, the integrated phase noise for frequencies above 70 mHz (< 14.2 s) is only 10 mrad. We then implement a PID control loop between the newly established detection scheme and the acousto-optic phase shifter (Fig. 2(a)) to actively compensate for slow drift in the CEP (Fig. 4(a)). To this end, we average time-sequences of about 1 s of the digitized data and calculate its deviation from $\varphi_{set} = 0$. This phase error signal is used to adjust the phase shifter and therefore the CEP. The blue line in Fig. 4(a) shows the measured CEP when the PID loop is active. The narrow histogram in Fig. 4(b) underlines the quality of the detection and control scheme. With the PID loop engaged, we reach a stability of $\sigma = 9.2$ mrad (integrated for 20.7 ms and acquired over 4.5 h), which is 30 times better than the free-running case. The main limitation of the control bandwidth currently is the implementation of the PID software, which is based on a Python script.

Optics EXPRESS

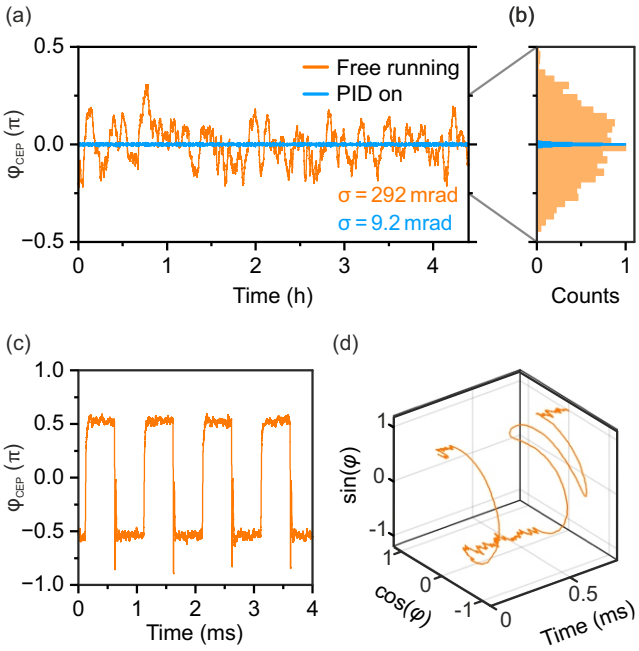

Fig. 4. CEP stabilization and control. (a) Recording the linear error signal over 4.5 h allows us to directly measure the CEP stability of the free-running laser system (orange). Each data point has been integrated for 20.7 ms. By sending the signal to a PID controller, the CEP can be actively stabilized (blue) with the acousto-optic phase shifter. (b) Histograms of the free running (orange) and stabilized (blue) laser reveals a CEP stability (σ) of 292 mrad and 9.2 mrad, respectively. (c) Square-wave CEP modulation at 1 kHz detected by f-$2f$ polarization interferometry. (d) Measurement data from (c) from 0 to 0.8 ms in the X-Y-plane before phase calculation. The large detection bandwidth allows us to trace the trajectory and reveal the switching behavior of the phase shifter.

Such feed-forward CEP control schemes employing AOMs can also operate at higher bandwidth as demonstrated successfully in the past [32]. Note, that with our technique every phase setpoint φ_{set} within 2π is reachable. For long-term drift, similar performance can be achieved with the conventional f-$2f$ interferometer and a spectrometer. However, our novel approach is easier to implement, can be faster, and does not require an expensive spectrometer.

In a second application, we apply a square wave modulation at 1 kHz to the phase of the driving voltage of the phase shifter. The CEP detected as a function of time (Fig. 4(c)) changes from $-\pi/2$ to $\pi/2$ with a period of 1 ms corresponding to an inversion of the waveform. For this measurement, the data was digitized at a sampling rate of 10 MS/s and the ADC is locked to the repetition rate with a 10 MHz reference signal. The above-described trivial steps were applied after the measurements to tag the CEP to every sampling point. No averaging is applied. On top of the plateaus, the signal shows tiny high-frequency CEP fluctuations. The sharp step edges are finely resolved such that differences between rising and falling edges are apparent. The rising edge increases monotonically within 10 µs (25% - 75% rise), which is in agreement with the speed of the photodiodes. These detection rates are on par with the currently best implementations for the conventional detection mechanisms and are only limited by the circuitry and choice of the photodiodes. In principle, detection rates as fast as the repetition rates of conventional laser oscillators operating in the range of tens of MHz can be achieved.

Optics EXPRESS

For closer inspection of the falling edges, we trace the CEP trajectory in the complex plane from 0 to 0.8 ms (Fig. 4(d)). In the CEP projection in panel c, the falling edge first overshoots the lower CEP value and then approaches -π/2 in a damped oscillation of a frequency of approximately 44 kHz. Depicting this trajectory in the complex plane further underpins this behavior in detail. We attribute the observed switching dynamics to ringing of the involved control electronics.

At this point, it is worth noting that the presented four-quadrant detection scheme would also allow for a combination of the two applications, i.e., stabilizing the long-term drift in the time-averaged phase of an arbitrarily short-term modulated CEP. We believe that this is particularly useful in combination with fast acousto-optic phase shifters, allowing for simultaneous control of CEP and offset frequency with a bandwidth up to the repetition rate [32]. In our proof-of-principle implementation, the photodiode signals are recorded with a fast analog-digital converter card (maximal rate: 125 MSa/s). Choosing a slow scripting language and slow photodiodes is the bottleneck of our setup and currently limits the real-time performance of our device. However, it can be easily improved to single-shot CEP detection at repetition rates of conventional laser oscillators and broadband correction by using high-bandwidth photodetectors, fast AD-sampling rates and implementations of the phase calculation, the moving average filter, the PID-loop, and the waveform generator in real-time electronics. The only computationally expensive step is given by the retrieval of the arctangent of two measured data points. Studies exist that show field-programmable gate array implementations of this operation with tens of MHz bandwidth, allowing for the proposed real-time detection [35].

In conclusion, we have presented a broadband four-quadrant CEP detection scheme that is based on f-$2f$ polarization interferometry. In a proof-of-principle measurement with pJ pulse energies, we demonstrated a linear CEP response for the full phase angle of 2π. Therefore, it has equal capabilities as the scheme presented in [27]. Our implementation utilizes a common-path geometry and is thus inherently drift free. Furthermore, the detection scheme is easy to set up and robust against minor deviations from the perfect configuration. The photodiode-based detection further promises single-shot detection speed at oscillator repetition rates. This opens up the possibility to perform CEP tagging of measured data, enabling CEP-sensitive experiments even with free-running oscillators. Additionally, in combination with dispersive wedges or acousto-optic modulators, the CEP of ultrashort laser pulses can be custom-tailored [32]. The scheme can also be employed to stabilize the time overlap from any spectrally coinciding, but cross-polarized beams [36]. This precision in waveform control paves the way to lightwave steering of electronic motion, with wide applicability from tailoring higher-order nonlinearities like the generation of attosecond pulses from HHG in gases [3–5], to the generation of attosecond electron wave packets from nanoantennas [11], or field-emitting nanotips [8,13], serving as a source for attosecond electron microscopy [37,38].

Funding. Deutsche Forschungsgemeinschaft (HU1598/8, 314695032, 406658631, 502572516).

Disclosures. C. T. and M. H. are employed by TOPTICA Photonics AG. C. T. is one of the inventors listed in the cited patent [33] that is relevant for the used laser system. The CEP detection scheme introduced in this publication is independent of the laser system. All other authors declare that there are no conflicts of interest related to this article.

Data availability. Data underlying the results presented in this paper are not publicly available at this time but may be obtained from the authors upon reasonable request.

Supplemental document. See Supplement 1 for supporting content.

References

1. E. Goulielmakis, V. S. Yakovlev, A. L. Cavalieri, *et al.*, "Attosecond control and measurement: lightwave electronics," Science **317**(5839), 769–775 (2007).
2. M. Ferray, A. L'Huillier, X. F. Li, *et al.*, "Multiple-harmonic conversion of 1064 nm radiation in rare gases," J. Phys. B **21**(3), L31–L35 (1988).
3. A. Baltuška, T. Udem, M. Uiberacker, *et al.*, "Attosecond control of electronic processes by intense light fields," Nature **421**(6923), 611–615 (2003).

Optics EXPRESS

4. I. J. Sola, E. Mével, L. Elouga, *et al.*, "Controlling attosecond electron dynamics by phase-stabilized polarization gating," Nat. Phys. **2**(5), 319–322 (2006).
5. F. Ferrari, F. Calegari, M. Lucchini, *et al.*, "High-energy isolated attosecond pulses generated by above-saturation few-cycle fields," Nat. Photonics **4**(12), 875–879 (2010).
6. M. Borsch, M. Meierhofer, M. Kira, *et al.*, "Lightwave electronics in condensed matter," Nat. Rev. Mater. **8**(10), 668–687 (2023).
7. C. P. Schmid, L. Weigl, P. Grössing, *et al.*, "Tunable non-integer high-harmonic generation in a topological insulator," Nature **593**(7859), 385–390 (2021).
8. B. Piglosiewicz, S. Schmidt, D. J. Park, *et al.*, "Carrier-envelope phase effects on the strong-field photoemission of electrons from metallic nanostructures," Nat. Photonics **8**(1), 37–42 (2014).
9. T. L. Cocker, D. Peller, P. Yu, *et al.*, "Tracking the ultrafast motion of a single molecule by femtosecond orbital imaging," Nature **539**(7628), 263–267 (2016).
10. P. D. Keathley, W. P. Putnam, P. Vasireddy, *et al.*, "Vanishing carrier-envelope-phase-sensitive response in optical-field photoemission from plasmonic nanoantennas," Nat. Phys. **15**(11), 1128–1133 (2019).
11. M. Ludwig, G. Aguirregabiria, F. Ritzkowsky, *et al.*, "Sub-femtosecond electron transport in a nanoscale gap," Nat. Phys. **16**(3), 341–345 (2020).
12. Y. Yang, M. Turchetti, P. Vasireddy, *et al.*, "Light phase detection with on-chip petahertz electronic networks," Nat. Commun. **11**(1), 3407 (2020).
13. P. Dienstbier, L. Seiffert, T. Paschen, *et al.*, "Tracing attosecond electron emission from a nanometric metal tip," Nature **616**(7958), 702–706 (2023).
14. G. Gallot and D. Grischkowsky, "Electro-optic detection of terahertz radiation," J. Opt. Soc. Am. B **16**(8), 1204–1212 (1999).
15. A. Leitenstorfer, A. Moskalenko, T. Kampfrath, *et al.*, "The 2023 terahertz science and technology roadmap," J. Phys. D: Appl. Phys. **56**(22), 223001 (2023).
16. G. G. Paulus, F. Grasbon, H. Walther, *et al.*, "Absolute-phase phenomena in photoionization with few-cycle laser pulses," Nature **414**(6860), 182–184 (2001).
17. T. Wittmann, B. Horvath, W. Helml, *et al.*, "Single-shot carrier–envelope phase measurement of few-cycle laser pulses," Nat. Phys. **5**(5), 357–362 (2009).
18. H. R. Telle, G. Steinmeyer, A. E. Dunlop, *et al.*, "Carrier-envelope offset phase control: A novel concept for absolute optical frequency measurement and ultrashort pulse generation," Appl. Phys. B **69**(4), 327–332 (1999).
19. D. J. Jones, S. A. Diddams, J. K. Ranka, *et al.*, "Carrier-envelope phase control of femtosecond mode-locked lasers and direct optical frequency synthesis," Science **288**(5466), 635–639 (2000).
20. M. Kakehata, H. Takada, Y. Kobayashi, *et al.*, "Single-shot measurement of carrier-envelope phase changes by spectral interferometry," Opt. Lett. **26**(18), 1436–1438 (2001).
21. T. Fordell, M. Miranda, C. L. Arnold, *et al.*, "High-speed carrier-envelope phase drift detection of amplified laser pulses," Opt. Express **19**(24), 23652–23657 (2011).
22. S. Mikaelsson, J. Vogelsang, C. Guo, *et al.*, "A high-repetition rate attosecond light source for time-resolved coincidence spectroscopy," Nanophotonics. **10**, 117–128 (2020).
23. M. Kurucz, S. Tóth, R. Flender, *et al.*, "Single-shot CEP drift measurement at arbitrary repetition rate based on dispersive fourier transform," Opt. Express **27**(9), 13387–13398 (2019).
24. T. Xian, W. Wang, and L. Zhan, "Dispersive Temporal Interferometry toward Single-Shot Probing Ultrashort Time Signal with Attosecond Resolution," Adv. Photonics Res. **3**(4), 2100303 (2022).
25. S. Koke, C. Grebing, B. Manschwetus, *et al.*, "Fast f-to-2f interferometer for a direct measurement of the carrier-envelope phase drift of ultrashort amplified laser pulses," Opt. Lett. **33**(21), 2545–2547 (2008).
26. A. Liehl, D. Fehrenbacher, P. Sulzer, *et al.*, "Ultrabroadband out-of-loop characterization of the carrier-envelope phase noise of an offset-free Er:fiber frequency comb," Opt. Lett. **42**(10), 2050–2053 (2017).
27. C. Guo, M. Miranda, A.-K. Raab, *et al.*, "Single-shot, high-repetition rate carrier-envelope-phase detection of ultrashort laser pulses," Opt. Lett. **48**(20), 5431–5434 (2023).
28. S. Pancharatnam, "Generalized theory of interference, and its applications," Proc. - Indian Acad. Sci., Sect. A **44**(5), 247–262 (1956).
29. B. Saleh and M. Teich, *Fundamentals of Photonics*, (John Wiley & Sons, Inc. 2007), Chap. 6.
30. H. Telle, "Verfahren zum Erzeugen eines Frequenzspektrums in Form eines Frequenzkamms und Lasereinrichtung hierfür," Deutsches Patent- und Markenamt DE 10 2019 129 337 B9 (01 December 2005).
31. G. Krauss, D. Fehrenbacher, D. Brida, *et al.*, "All-passive phase locking of a compact Er:fiber laser system," Opt. Lett. **36**(4), 540–542 (2011).
32. S. Koke, C. Grebing, H. Frei, *et al.*, "Direct frequency comb synthesis with arbitrary offset and shot-noise-limited phase noise," Nat. Photonics **4**(7), 462–465 (2010).
33. T. Puppe, C. Tresp, M. Eisele, *et al.*, "Laservorrichtung zur Erzeugung eines optischen Frequenzkamms," Deutsches Patent- und Markenamt DE 10 2019 129 337 B9 (20 May 2021).
34. G. Krauss, S. Lohss, T. Hanke, *et al.*, "Synthesis of a single cycle of light with compact erbium-doped fibre technology," Nat. Photonics **4**(1), 33–36 (2010).
35. R. Gutierrez, V. Torres, and J. Valls, "FPGA-implementation of atan(Y/X) based on logarithmic transformation and LUT-based techniques," J. Syst. Archit. **56**(11), 588–596 (2010).

Optics EXPRESS

36. M. Meierhofer, S. Maier, D. Afanasiev, *et al.*, "Interferometric carrier-envelope phase stabilization for ultrashort pulses in the mid-infrared," Opt. Lett. **48**(5), 1112–1115 (2023).
37. D. Nabben, J. Kuttruff, L. Stolz, *et al.*, "Attosecond electron microscopy of sub-cycle optical dynamics," Nature **619**(7968), 63–67 (2023).
38. H. Y. Kim, M. Garg, S. Mandal, *et al.*, "Attosecond field emission," Nature **613**(7945), 662–666 (2023).